Bol. Soc. Paran. Mat.
©SPM – E-ISSN-2175-1188
SPM: www.spm.uem.br/bspm

(3s.) **v. 2026 (44) 3** : 1–14.
ISSN-0037-8712
doi:10.5269/bspm.80308

A Hybrid Model Combining Anisotropic Diffusion and Variable-Order Total Variation for Poisson Denoising

Anouar Ben-Loghfyry[1] and Youness El Yazidi[2]

ABSTRACT: In this paper, we present and analyze a new model for Poisson denoising, integrating variable-order fractional derivatives with anisotropic diffusion. The unique challenge of Poisson image denoising lies in its dependence on image intensity, which introduces significant complexities in the restoration process. The intricate geometry of natural images demands robust regularization techniques that can preserve fine details and maintain piecewise smooth regions. To achieve this, we employ a variable-order approach that adapts to image features and an anisotropic diffusion term that accommodates directional variations within the image. For the numerical solution, we implement the Alternating Direction Method of Multipliers (ADMM) algorithm, a powerful tool for handling complex optimization problems. Extensive experimental results highlight the effectiveness of our method, demonstrating marked improvements over existing state-of-the-art techniques for denoising images corrupted by Poisson noise.

Keywords: Fractional derivative, variable-order, image Poisson denoising, minimization.

Contents

1. Introduction

In real world applications, the appearance of the Poisson noise is seen due to the statistical behavior of electromagnetic waves such as positron emission tomography, astronomical imaging x-rays, visible lights, gamma rays [9,18,32]. For instance, the x-ray and gamma sources can emit a certain number of photons. These sources have a random fluctuation considered as a Poisson distribution. In image processing especially with Poisson noise type, even if the peak value is smaller, the image will be noisier.

In general, Poisson denoising models seek to reconstruct a clean image u based on the knowledge of a observed noisy image f by solving the next problem

$$\min_u \int_\Omega (u - f \log u)\, dx$$

where $\Omega \subset \mathbb{R}^2$ is assumed to be the image domain.

2020 *Mathematics Subject Classification:* 35K15, 35R30, 65D12, 90C53.
Submitted November 22,2025. Published June 05, 2026

Nowadays, many regularization approaches have been presented and investigated in the case of Poisson denoising field, including Tikhonov regularization [31], Total Variation approaches (TV) [7,28]. This latter aims to solve the following problem

$$\min_u \int_\Omega |\nabla u| + \beta(u - f\log u))dx \tag{1.1}$$

where $\beta > 0$ is a regularization parameter. In literature, there exist efficient algorithms for solving Poisson denoising model based on TV-regularized (1.1), we mention for example: a primal-dual algorithm [34], an alternating extra-gradient method [3], the well-known split Bregman method [20], and an augmented Lagrangian method [14,10].

It is wildly known that the TV-based models can perform well by seeking piecewise constant images for preserving edges and corners while removing the noise. But it has many drawbacks, such as the staircasing effects and the loss of image contrasts [21]. To remedy these problems, some high-order regularization terms in the Gaussian noise case have been presented, including anisotropic total variation regularization [2,6], non-local TV model [16], a generalized version of TV regularization in [5].

In terms of fractional calculus, the fractional-order total variation (FOTV) is a generalization of TV based models. Simulation results have shown that FOTV is able to fix the infamous drawbacks of staircasing and speckle artifacts [1], as an advantage of the non-local property of fractional calculus. The FOTV based models show also an important propriety, preserving features, edges and corners. For instance, the FOTV can keep image contrasts [35] and preserve textures [26]. FOTV regularization approach has been also applied in other situations such as image denoising in Gaussian noise case [8,35,15] and in super-resolution field [17]. However, in this paper we introduce a variable-order fractional total variation, which is generally a novelty in image processing. The idea behind this choice lays, as mentioned above, in the effectiveness of the fractional derivative. Another reason for this choice is that the variable order FOTV extends and generalizes the famous models TV and TV^2 for values in $(1, 2)$ (see [15]). The modeling process with this tool shows great results in real world applications especially the memory characteristics of variable-order operators [24].

A novel attempt in this work lays in the anisotropic total variation regularization [2,6]. This term was originally extracted from the PDE of Weickert [33]. This PDE shows a great performance in many image processing fields, specially in facing the Staicasing effect and speckle artifacts.

The main contributions of this work lay in combining two novel models, the first is based on FOTV with a variable order [15] and an anisotropic model based on Weickert model [33]. The combined model is novelty in the field of Poisson denoising qnd in image processing. Besides to implementing the ADMM algorithm for this kind of problems.

This paper is organized as follows. We begin in Section 2 by introducing the proposed model and reviewing key formulas for fractional derivatives, covering both constant and variable-order cases for comparison. In Section 3, we detail our finite difference approach for discretizing these derivatives and then formulate the ADMM algorithm. Section 4 presents numerical simulations to illustrate our results, and we offer concluding remarks in Section 5.

2. The proposed approach

Our proposed model integrates a variable-order derivative with anisotropic total variation. The model takes the following form:

$$\min_u \left\{ \gamma_1(x)\ TV^{\hat{\alpha}}(u) + \gamma_2(x) \int_\Omega \nabla u^T D(f) \nabla u dx + \gamma_3(x) \int_\Omega (u - f\log u)dx \right\} \tag{2.1}$$

where $\gamma_i(x)$ for $i = 1, 2, 3$ are the regularization parameters, verifying $\gamma_1(x) + \gamma_2(x) + \gamma_3(x) = 1$ and the function $\hat{\alpha}$ varies with respect to the norm of x and $1 \leq \hat{\alpha} \leq 2$. The diffusion matrix D will be discussed in the next subsection(2.1).

In our model (2.1), we have two regularization terms. The first term $TV^{\hat{\alpha}}(u)$ is the Total Variation model based on the fractional variable-order derivative. In literature, it is known that the fractional calculus has potentials, especially in image processing [15]. In the case of fractional derivatives, implementing

this tools as a regularization term leads to improve the reconstruction quality of image by preserving edges and corners, and also leads to enforce a reduced smoothness compared to famous regularizations such as TV. The second term in (2.1) is an anisotropic total variation regularization based on diffusion tensor. The idea behind this term is to try to combine the benefits of anisotropic filtering approach the well-known Weickert model [33] and the known total variation. Which is famous for its noise deleting quality.

It is clear that our model composition is based on two major ideas. The first is the use of a term that can preserve features and control smoothness. Another term that can easily delete noises in a robust way. The denoising procedure of our model is to start by the second regularization term in order to detect the characteristics of the observed image. The result image will still be noisy but perfect to denoise thanks to the anisotropic total variation which we will mention in the ADMM algorithm.

2.1. preliminary

In this section, we introduce the seminorm $TV^{\hat{\alpha}}$. For all $1 \leq \hat{\alpha} \leq 2$ and $x \in \Omega$, we introduce the space $\mathcal{C}_0^{\hat{\alpha}}(\Omega)$ of $\hat{\alpha}$-order continuous and differentiable with a compact support functions on Ω. Thereafter, the total variation of $\hat{\alpha}$-order reads

$$TV^{\hat{\alpha}}(u) = \sup\left\{\int_\Omega u \operatorname{div}^{\hat{\alpha}} \varphi dx : \varphi = (\varphi_1, \varphi_2) \in \left(\mathcal{C}_0^{\hat{\alpha}}(\Omega)\right)^2, |\varphi_i|_{L^\infty(\Omega)} \leq 1, i = 1, 2\right\},$$

and the divergence of $\hat{\alpha}$-order is defined as follows

$$\operatorname{div}^{\hat{\alpha}} \varphi = \frac{\partial^{\hat{\alpha}} \varphi_1}{\partial x^{\hat{\alpha}}} + \frac{\partial^{\hat{\alpha}} \varphi_2}{\partial y^{\hat{\alpha}}}$$

To this end, the bounded functions of $\hat{\alpha}$-order TV space, is defined by

$$BV^{\hat{\alpha}}(\Omega) := \left\{u \in L^1(\Omega) : TV^{\hat{\alpha}}(u) < \infty\right\}.$$

Moving to the second regularization term. $D = D(J_\rho(\nabla^\alpha f_\sigma))$ is an anisotropic diffusion tensor and J_ρ is its structure, which is given by

$$J_\rho(\nabla^\alpha f_\sigma) = G_\rho * (\nabla^\alpha f_\sigma \otimes \nabla^\alpha f_\sigma) = G_\rho * (\nabla^\alpha (G_\sigma * f) \times \nabla^\alpha (G_\sigma * f)^T), \tag{2.2}$$

where ∇^α is defined as the fractional constant-order Grunwald-Letnikov derivative, with G_ρ and G_σ are Gaussian convolution kernels given by $G_\tau = \frac{1}{2\pi\tau^2} \exp(-\frac{|x|^2}{2\tau^2})$.

Defining the diffusion tensor D, recognize an eigenvalue decomposition of the tensor J_ρ that we can express it via an orthogonal matrix as $V \in \mathbb{R}^{2\times 2}$ by $J_\rho = V^T \Sigma V$, where $\Sigma := \operatorname{diag}(\lambda_+, \lambda_-) \in \mathbb{R}^{2\times 2}$ A diagonal matrix, λ_+ and λ_+ represents the tensor J_ρ eigenvalues. Those latter are given by the next

$$\lambda_{+/-} = \frac{1}{2}\left(trace(J_\rho) \pm \sqrt{trace^2(J_\rho) - 4det(J_\rho)}\right) \tag{2.3}$$

From another side, the diffusion tensor D is expressed by

$$x \in D : \Omega \mapsto V^T(x) \operatorname{diag}\left(\theta\left(\lambda_+(x) - \lambda_-(x)\right), 1\right) V(x) \tag{2.4}$$

with

$$\theta(s) := \left(1 + \frac{s^2}{\theta_0}\right)^{-1} \tag{2.5}$$

for some threshold $\theta_0 > 0$.
This choice is based on the geometric proprieties observed in the image. Indeed, if $\lambda_{+/-} \approx 0$, The smoothing behaves isotropically in homogeneous regions, which are areas where u is nearly constant. While if $\lambda_+ \gg \lambda_- \approx 0$ (or $\lambda_- \gg \lambda_+ \approx 0$), the smoothing process is anisotropic and oriented along the edges. However, if $\lambda_+ \gg \lambda_- \gg 0$, the smoothing goes into corners.

The function θ in (2.5) is chosen carefully in order to satisfy the following constraints:

- Isotropic: in the homogeneous zones (u is almost constant), the diffusion process will be isotropic.
- Anisotropic: close to corners and edges, the diffusion process is anisotropic.

3. Discretization and ADMM algorithm

We start by introducing the variable order derivative tools and the discretization of the diffusion matrix D using the finite difference method.

3.1. Fractional variable order derivatives

To simplify the presentation, let's first examine the 1D case. We consider a function f defined on $[a, b] \subset \mathbb{R}$ and a fractional order α from $\mathbb{R}^+$.
We use the standard constant-order Grunwald-Letnikov derivative, defined as [25]. We introduce the constant-order fractional derivative as follows:

$$ {}^{G}_{a}D^{\alpha}_{x} f(x) = \lim_{h\to 0} \frac{1}{h^{\alpha}} \sum_{j=0}^{[\frac{x-a}{h}]} (-1)^j \binom{\alpha}{j} f(x - jh), $$

Where :

$$ \binom{\alpha}{j} = \frac{\alpha(\alpha-1)\dots(\alpha-j+1)}{j!}. $$

This definition describes the left-sided constant-order fractional derivative.
Now, we move to a valuable properties about the recursive fractional derivative definitions.

Definition 1 *We define the $\mathcal{B}$-type fractional variable order derivative as next*

$$ {}^{\mathcal{B}}_{a}D^{\alpha(x)}_{x} f(x) = \lim_{h\to 0} \sum_{j=0}^{[\frac{x-a}{h}]} \frac{(-1)^j}{h^{\alpha(x-jh)}} \binom{\alpha(x-jh)}{j} f(x - jh) $$

The $\mathcal{B}$-type fractional variable-order can be expressed in discrete form as next:

$$ {}^{\mathcal{B}}\Delta^{\alpha_l} f_l = \sum_{j=0}^{l} \frac{(-1)^j}{h^{\alpha_{l-j}}} \binom{\alpha_{l-j}}{j} f_{l-j} $$

Here, $l = 0, 1, ..., M$, and f_l represents the l-th element of the discrete function f.

Remark 1 *The $\mathcal{B}$-type definition calculates the coefficients for past samples using the fractional order that was present at each of those locations.*

Another definition proposed in [23] offers a recursive alternative, which was mainly derived from the previous definition. It is given by:

Definition 2 *We define the $\mathcal{E}$-type fractional variable order derivative by*

$$ {}^{\mathcal{E}}_{a}D^{\alpha(x)}_{x} f(x) = \lim_{h\to 0} \left(\frac{f(x)}{h^{\alpha(x)}} - \sum_{j=1}^{[\frac{x-a}{h}]} (-1)^j \binom{-\alpha(x-jh)}{j} \frac{h^{\alpha(x-jh)}}{h^{\alpha(x)}} \; {}^{\mathcal{E}}_{a}D^{\alpha(x)}_{x-jh} f(x) \right) $$

Following the same logic as the $\mathcal{B}$-type, the discrete form of the $\mathcal{E}$-type fractional variable-order derivative is given as:

$$ {}^{\mathcal{E}}\Delta^{\alpha_l} f_l = \frac{f_l}{h^{\alpha_l}} - \sum_{j=1}^{l} (-1)^j \binom{-\alpha_{l-j}}{j} \frac{h^{\alpha_{l-j}}}{h^{\alpha_l}} \; {}^{\mathcal{E}}\Delta^{\alpha_{l-j}} f_{l-j} \tag{3.1} $$

where $l = 1, ..., M$.

Remark 2 *In the special case of a constant order (i.e., $\alpha(x) = const$), all three definitions coincide and simplify to the standard constant-order derivative:*

$$ {}^{G}_{a}D^{\alpha}_{x} f(x) \;=\; {}^{\mathcal{B}}_{a}D^{\alpha}_{x} f(x) \;=\; {}^{\mathcal{E}}_{a}D^{\alpha}_{x} f(x) $$

Now, we aim to establish the discrete form associated to $\mathcal{E}$-type fractional variable-order derivative [22].

Theorem 1 *The fractional operator $\mathcal{E}$-type stated in (3.1) has a discrete form expressed as next*

$$\begin{pmatrix} {}_{\mathcal{E}}\Delta^{\alpha_0} f_0 \\ {}_{\mathcal{E}}\Delta^{\alpha_1} f_1 \\ \vdots \\ \vdots \\ {}_{\mathcal{E}}\Delta^{\alpha_N} f_N \end{pmatrix} = \mathcal{D}_0^N \begin{pmatrix} f_0 \\ f_1 \\ \vdots \\ \vdots \\ f_N \end{pmatrix} \tag{3.2}$$

where

$$\mathcal{D}_0^N = \mathcal{D}(\alpha_N, N) \dots \mathcal{D}(\alpha_1, 1)\mathcal{D}(\alpha_0, 0), \tag{3.3}$$

and

$$\mathcal{D}(\alpha_r, r) = \left(\begin{array}{c|c|c} I_{r,r} & 0_{r,1} & 0_{r,N-r} \\ \hline q_r & h^{-\alpha_r} & 0_{1,N-r} \\ \hline 0_{N-r,r} & 0_{N-r,1} & I_{N-r,N-r} \end{array}\right), \quad \textit{for all } r = 0, 1, \dots, M$$

$$(q_r)_m = (-1)^{r-m+1} \binom{-\alpha_{m-1}}{r-m+1}$$

3.2. Diffusion matrix discretization

Let the image domain Ω be partitioned by a grid (x_k, y_l), where $k = 0, ..., N+1$ and $l = 0, ..., M+1$. We perform our discretization along the x-direction at the inner grid points, corresponding to $k = 1, ..., N$ and $l = 1, ..., M$.

There are different approaches in the literature to perform discretization of $\operatorname{div}(D\nabla\psi)$ term. We rewrite the fractional diffusion matrix in (2.4)

$$D := V^T(x) \operatorname{diag}\left(\theta\left(\lambda_+(x) - \lambda_-(x)\right), 1\right) V(x)$$

The discretization of the operator D is trivial. Furthermore, the eigenvalues are calculated as in (2.3). For simplicity reasons, we denote:

$$D = \begin{pmatrix} a & b \\ b & c \end{pmatrix}$$

Now, we compute $\operatorname{div}(D\nabla\psi)$,

$$\begin{aligned} \operatorname{div}(D\nabla\psi) &= \operatorname{div}\left[\begin{pmatrix} a & b \\ b & c \end{pmatrix}\begin{pmatrix} \partial_x\psi \\ \partial_y\psi \end{pmatrix}\right] \\ &= \partial_x(a\partial_x\psi) + \partial_x(b\partial_y\psi) + \partial_y(b\partial_x\psi) + \partial_y(c\partial_y\psi) \\ &= \partial_x a\ \partial_x\psi + a\ \partial_{xx}\psi + \partial_x b\ \partial_y\psi + b\ \partial_{xy}\psi \\ &+ \partial_y b\ \partial_x\psi + b\ \partial_{yx}\psi + \partial_y c\partial_y\psi + c\ \partial_{yy}\psi \end{aligned}$$

where $\partial_x u$ and $\partial_x u$ are given by

$$(\partial_x\psi)_{i,k} = \begin{cases} \psi_{i+1,k} - \psi_{i,k} & \text{if } i < N \\ 0 & \text{if } i = N \end{cases}$$

$$(\partial_y\psi)_{i,k} = \begin{cases} \psi_{i,k+1} - \psi_{i,k} & \text{if } k < M \\ 0 & \text{if } k = M \end{cases}$$

Also for the second derivatives:

$$(\partial_{xx}\psi)_{i,k} = \begin{cases} \psi_{i+1,k} - 2\psi_{i,k} + \psi_{i-1,k} & \text{if } 1 < i < N \\ \psi_{i+1,k} - \psi_{i,k} & \text{if } i = 1 \\ \psi_{i-1,k} - \psi_{i,k} & \text{if } i = N \end{cases}$$

$$(\partial_{yy}\psi)_{i,k} = \begin{cases} \psi_{i,k+1} - 2\psi_{i,k} + \psi_{i,k-1} & \text{if } 1 < k < M \\ \psi_{i,k+1} - \psi_{i,k} & \text{if } k = 1 \\ \psi_{i,k-1} - \psi_{i,k} & \text{if } k = N \end{cases}$$

$$(\partial_{xy}\psi)_{i,k} = \begin{cases} \psi_{i,k+1} - \psi_{i,k} + \psi_{i-1,k+1} + \psi_{i-1,k} & \text{if } 1 < i < N,\ 1 < k < M \\ 0 & \text{if } i = 1 \\ 0 & \text{if } i = N \end{cases}$$

$$(\partial_{xy}\psi)_{i,k} = \begin{cases} \psi_{i+1,k} - \psi_{i,k} + \psi_{i+1,k-1} + \psi_{i,k-1} & \text{if } 1 < i < N,\ 1 < k < M \\ 0 & \text{if } k = 1 \\ 0 & \text{if } k = M \end{cases}$$

Based of the foregoing quantities, the divergence operator $\mathrm{div}(D\nabla\psi)$ can be expressed in a new form as

$$\begin{aligned}[(\nabla)^*\,(D(f)\nabla\psi)]_{i,k} = {} & (\partial_x a)_{i,k}\ (\partial_x\psi)_{i,k} + a_{i,k}\ (\partial_{xx}\psi)_{i,k} + (\partial_x b)_{i,k}\ (\partial_y\psi)_{i,k} + b_{i,k}\ (\partial_{xy}\psi)_{i,k} \\ & + (\partial_y b)_{i,k}\ (\partial_x\psi)_{i,k} + b_{i,k}\ (\partial_{yx}\psi)_{i,k} + (\partial_y c)_{i,k}(\partial_y\psi)_{i,k} + c_{i,k}\ (\partial_{yy}\psi)_{i,k}. \quad (3.4)\end{aligned}$$

The discretization of (3.4) at any inner point (i, j) is equivalent to convolving the image u with a 3×3 array, often called a stencil. For the numerical scheme to be stable, Weickert's condition was that every element of the diffusion matrix must be positive. The standard discretization (3.4) doesn't guarantee this, though. To fix this, Weickert [33] proposed a new non-negative discretization, which we've summarized in Table (1).

$\frac{\lvert b_{k-1,l-1}\rvert - b_{k-1,l-1}}{4}$ $+\frac{\lvert b_{k,l}\rvert - b_{k,l}}{4}$	$\frac{c_{k,l+1}+c_{k,l}}{2} - \frac{\lvert b_{k,l+1}\rvert + \lvert b_{k,l}\rvert}{2}$	$\frac{\lvert b_{k+1,l+1}\rvert + b_{k+1,l+1}}{4}$ $+\frac{\lvert b_{k,l}\rvert + b_{k,l}}{4}$
$\frac{a_{k-1,l} + a_{k,l}}{2}$ $-\frac{\lvert b_{k-1,l}\rvert + \lvert b_{k,l}\rvert}{2}$	$-\frac{a_{k-1,l} + 2a_{k,l} + a_{k+1,l}}{2}$ $-\frac{\lvert b_{k-1,l-1}\rvert - b_{k-1,l-1} + \lvert b_{k+1,l+1}\rvert + b_{k+1,l+1}}{4}$ $-\frac{\lvert b_{k-1,l-1}\rvert + b_{k-1,l-1} + \lvert b_{k+1,l-1}\rvert - b_{k+1,l-1}}{4}$ $-\frac{\lvert b_{k-1,l}\rvert + \lvert b_{k+1,l}\rvert + \lvert b_{k,l-1}\rvert + \lvert b_{k,l+1}\rvert + 2\lvert b_{k,l}\rvert}{2}$ $-\frac{c_{k,l-1}+2c_{k,l}+c_{k,l+1}}{2}$	$\frac{a_{k+1,l} + a_{k,l}}{2}$ $-\frac{\lvert b_{k+1,l}\rvert + \lvert b_{k,l}\rvert}{2}$
$\frac{\lvert b_{k-1,l-1}\rvert + b_{k-1,l-1}}{4}$ $+\frac{\lvert b_{k,l}\rvert + b_{k,l}}{4}$	$\frac{c_{k,l-1}+c_{k,l}}{2} - \frac{\lvert b_{k,l-1}\rvert + \lvert c_{k,l}\rvert}{2}$	$\frac{\lvert b_{k+1,l-1}\rvert - b_{k+1,l-1}}{4}$ $+\frac{\lvert b_{k,l}\rvert - b_{k,l}}{4}$

Table 1: Non-negative discretization stencil

We denote by $A(u)$ the matrix containing the elements of the operator $\mathrm{div}(D\nabla u)$. Let S be the 3×3 matrix whose components are given in Table (1):

$$S = \begin{pmatrix} s_{11} & s_{12} & s_{13} \\ s_{21} & s_{22} & s_{23} \\ s_{31} & s_{32} & s_{33} \end{pmatrix}$$

For a fixed point (i, j), the term $[A(u)]_{i,j}$ is calculated as follows:

$$\begin{aligned}[A(u)]_{i,j} = {} & u_{i-1,j-1}\ s_{11} + u_{i-1,j}\ s_{12} + u_{i-1,j+1}\ s_{13} \\ & + u_{i,j-1}\ s_{21} + u_{i,j}\ s_{22} + u_{i,j+1}\ s_{23} \\ & + u_{i+1,j-1}\ s_{31} + u_{i+1,j}\ s_{32} + u_{i+1,j+1}\ s_{33}\end{aligned}$$

which conclude the discretization with $(\nabla)^*\,(D(f)\nabla u)$.

3.3. ADMM algorithm

Having established the discrete forms of the variable-order derivative and the diffusion matrix, we now apply the ADMM algorithm. For the numerical implementation, we consider the following discretized version of the Poisson denoising model (2.1):

$$\min_{u\in\mathbb{R}^{N\times M}} \gamma_1(x)\left\|\nabla^{\hat{\alpha}}u\right\|_1+\gamma_2(x)\left\langle D(f)\nabla u,\nabla u\right\rangle+\gamma_3(x)\left\langle u-f\log u,\mathbf{1}_\Omega\right\rangle$$

where $\mathbf{1}_\Omega$ denotes the indicator function on a discrete grid of the image domain Ω.

Remark 3.1 $\gamma_{1,2,3}(x)$ are taken as constant parameters.

To solve the proposed model (2.1), we employ the alternating direction method of multipliers (ADMM) [4,13]. We first introduce an auxiliary variable $\mathbf{z}$ to reformulate (2.1) as:,

$$\min_{u,\mathbf{z}}\ \gamma_1\|\mathbf{z}\|_1+\gamma_2\left\langle\nabla u^T D(f)\nabla u,\mathbf{1}_\Omega\right\rangle+\gamma_3\left\langle u-f\log u,\mathbf{1}_\Omega\right\rangle\quad\text{s.t.}\quad\mathbf{z}=\nabla^{\hat{\alpha}}u \tag{3.5}$$

The augmented Lagrangian functional associated to (3.5) reads

$$\mathcal{L}(u,\mathbf{z};\boldsymbol{\lambda})=\gamma_1\|\mathbf{z}\|_1+\left\langle\boldsymbol{\lambda},\mathbf{z}-\nabla^{\hat{\alpha}}u\right\rangle+\frac{\mu}{2}\left\|\mathbf{z}-\nabla^{\hat{\alpha}}u\right\|_2^2+\gamma_2\left\langle\nabla u^T D(f)\nabla u,\mathbf{1}_\Omega\right\rangle+\gamma_3\left\langle u-f\log u,\mathbf{1}_\Omega\right\rangle \tag{3.6}$$

where $\boldsymbol{\lambda}$ is the Lagrangian multiplier and μ is a positive parameter. The ADMM algorithm is then given by the following subproblems:

$$\begin{cases} u^{k+1}=\underset{u}{\operatorname{argmin}}\ \mathcal{L}\left(u,\mathbf{z}^k;\boldsymbol{\lambda}^k\right),\\ \mathbf{z}^{k+1}=\underset{\mathbf{z}}{\operatorname{argmin}}\ \mathcal{L}\left(u^{k+1},\mathbf{z};\boldsymbol{\lambda}^k\right),\\ \boldsymbol{\lambda}^{k+1}=\boldsymbol{\lambda}^k+\mu\left(\mathbf{z}^{k+1}-\nabla^{\hat{\alpha}}u^{k+1}\right). \end{cases} \tag{3.7}$$

To solve the u-subproblem (3.7), we consider its Euler-Lagrange equation. With respect to u, this equation takes the form:

$$-\left(\nabla^{\hat{\alpha}}\right)^*\boldsymbol{\lambda}^k-\mu\left(\nabla^{\hat{\alpha}}\right)^*\left(\mathbf{z}^k-\nabla^{\hat{\alpha}}u\right)+2\ \gamma_2\ (\nabla u)^*\left(D(f)\nabla u\right)+\gamma_3\frac{(u-f)}{u}=0 \tag{3.8}$$

To handle the nonlinearity in (3.8), we use a fixed-point approach. We replace u in the denominator and in the anisotropic TV term with u^k. The update u^{k+1} is then found by solving the resulting linear equation with the FFT, assuming periodic boundary conditions. u^{k+1} is given by:

$$u^{k+1}=\mathcal{F}^{-1}\left(\frac{\mathcal{F}\left[\gamma_3 f+\mu u^k\circ\left(\nabla^{\hat{\alpha}}\right)^*\boldsymbol{\lambda}^k+u^k\circ\left(\nabla^{\hat{\alpha}}\right)^*\mathbf{z}^k+2\gamma_2 u^k\circ(\nabla)^*\left(D(f)\nabla u\right)\right]}{\gamma_3+\mu u^k\circ(\nabla u)^*\mathcal{F}\left(\left(\nabla^{\hat{\alpha}}\right)^*\right)\mathcal{F}\left(\nabla^{\hat{\alpha}}\right)}\right), \tag{3.9}$$

where $(\nabla)^*\left(D(f)\nabla u\right)$ is given in (3.4), $\nabla^{\hat{\alpha}}$ is stated in (3.2) and $\mathcal{F}$ is the Fourier transform and $\circ$ is component-wise multiplication. While the iterations in (3.9) are needed to approximate the solution for (3.8), the z-subproblem has a direct, closed-form solution:

$$\mathbf{z}^{k+1}=\text{shrink}\left(\nabla^{\hat{\alpha}}u^{k+1}-\frac{\boldsymbol{\lambda}^k}{\mu},\frac{1}{\mu}\right)$$

where $\text{shrink}(s,\xi):=\text{sgn}(s)\max\{|s|-\xi,0\}$. We summarize the complete ADMM algorithm for our Poisson denoising model in Algorithm (1).

Algorithm 1 The proposed ADMM approach

Inputs:

f observed noisy image.

Choose $\hat{\alpha}, \beta, \mu, \epsilon, \gamma_{1,2,3}$

Initialize:

$\boldsymbol{z}^0 = \mathbf{0}, \boldsymbol{\lambda}^0 = \mathbf{0}, u^0 = f$

While:

$\frac{\|u^{k+1}-u^k\|}{\|u^k\|} < \epsilon$

Do:

$$u^{k+1} = \mathcal{F}^{-1}\left(\frac{\mathcal{F}\left[\gamma_3 f + \mu u^k \circ \left(\nabla^{\hat{\alpha}}\right)^* \boldsymbol{\lambda}^k + u^k \circ \left(\nabla^{\hat{\alpha}}\right)^* \mathbf{z}^k + 2\gamma_2 u^k \circ (\nabla)^* \left(D(f)\nabla u\right)\right]}{\gamma_3 + \mu u^k \circ (\nabla u)^* \mathcal{F}\left(\left(\nabla^{\hat{\alpha}}\right)^*\right) \mathcal{F}\left(\nabla^{\hat{\alpha}}\right)}\right),$$

$$\mathbf{z}^{k+1} = \text{shrink}\left(\nabla^{\hat{\alpha}} u^{k+1} - \frac{\boldsymbol{\lambda}^k}{\mu}, \frac{1}{\mu}\right) \quad \boldsymbol{\lambda}^{k+1} = \boldsymbol{\lambda}^k + \mu\left(\mathbf{z}^{k+1} - \nabla^{\hat{\alpha}} u^{k+1}\right)$$

$\mathrm{k} = \mathrm{k} + 1$

4. Numerical results and discussions

In this section, we present the numerical results to show the effectiveness of our approach compared to existing Poisson restoration models. We compare our proposed model with TV^{α} models using various values of α. A quick note on our setup: we use the ADMM algorithm for the comparison models. All tests were performed in Matlab 2018 on a computer with a 3 GHz processor and 16 Gb of RAM. We check the performance of the models by measuring the PSNR and SSIM of the restored images. The PSNR metric is defined as follow:

$$\text{PSNR}(A, B) = 10\log_{10}\frac{K^2}{\frac{1}{MN}\sum_{i=1}^{M}\sum_{j=1}^{N}\left(A_{i,j} - B_{i,j}\right)^2}$$

Here, K represents the original image U maximum peak value's, and V is the recovered image. Calculating the SSIM starts with the local similarity index (ssim), which is computed between two small patches, u and v,

$$\text{ssim}(u, v) = \frac{\left(2\mu_u\mu_v + c_1\right)\left(2\sigma_{uv} + c_2\right)}{\left(\mu_u^2 + \mu_v^2 + c_1\right)\left(\sigma_u^2 + \sigma_v^2 + c_2\right)}$$

where μ_u/σ_u^2 and μ_v/σ_v^2 are the average and variance of u and v respectively, and σ_{uv} is their covariance. c_1 and c_2 are positive coefficients that just keep the denominator from being zero. The global SSIM is the mean of all these local ssim values.

$$\text{SSIM}(U, V) = \frac{1}{L}\sum_{k=1}^{L}\text{ssim}\left(u_k, v_k\right)$$

with u_k and v_k being the corresponding patches and L as the total number of patches.

4.1. Results comparisons

Poisson noise is known to depend on the original image's peak intensity. Because of this, we will test the performance of different Poisson denoising methods using a noise level of 55.
While other peak values (like 55, 155, or 255) are possible, we restricted our tests to 55. This is because a lower peak value results in a significantly noisier image, as Figure 1 illustrates, providing a better stress

test for our model's robustness. The reconstructed synthetic image used in the first figure 1 has the following form, for any $(x, y) \in [-50, 50] \times [-50, 50]$

$$u(x, y) = |x|^a + |y|^{0.8} \tag{4.1}$$

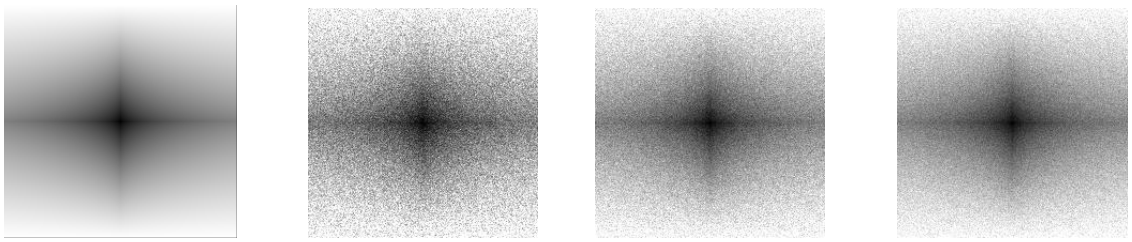

(a) Original image (b) Peak = 55 (c) Peak = 155 (d) Peak = 255

Figure 1: Different peak values of the image u defined in (4.1)

For the synthetic image, the optimal value of the fractional order for denoising is $\alpha = a + 1 = 1.8$. The denoising results for the synthetic image (4.1) are shown in Figure 2. We compare the results for $\alpha = 1.8$ and $\alpha = 1$ (the TV model). Other test images are shown in the figures (3)-(6). They present the denoising results at peak 55 using zoom-in patch to simplify the analysis later. The results are made by our approach and the TV^α models with $\alpha \in (1, 2)$. The values were taken differently, for $\beta \in \{4, 7, 9, 12\}$, for θ_0 in the diffusion matrix (2.5), we took $\theta_0 = 50$, for $\gamma_{1,2,3}$ in (2.1) we manage with $\gamma_1 = \frac{1}{peak}$ while verifying $\gamma_1 + \gamma_2 + \gamma_3 = 1$ and finally for the values of σ and ρ in (2.2), we took $\sigma = 1.5$ and $\rho = 4.5$.

Remark 4.1 The fractional variable order $\hat{\alpha}$ was chosen numerically based on obtained values in PSNR and SSIM. In future works, to obtain optimal values of $\hat{\alpha}$, one can employ heuristic methods for example [11,12].

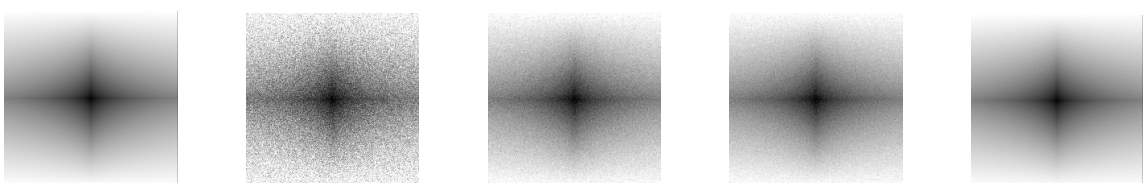

(a) Original (b) peak = 55 (c) TV [19] (d) TV^α [27] (e) Ours

Figure 2: Comparison results of Poisson denoising using the synthetic image (4.1) with peak at 55

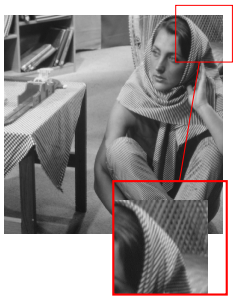

(a) Original image

(b) peak = 55

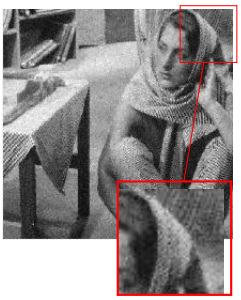

(c) TV [19]

(d) TV^{α} model [27]

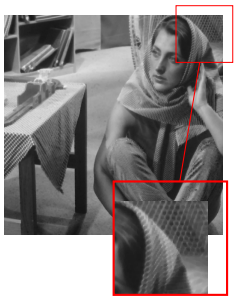

(e) Our approach

Figure 3: Comparison results of Poisson denoising using *Barbara image with peak at 55*

(a) Original image

(b) peak = 55

(c) TV [19]

(d) TV^{α} model [27]

(e) Our approach

Figure 4: Comparison results of Poisson denoising using *Cameraman image with peak at 55*

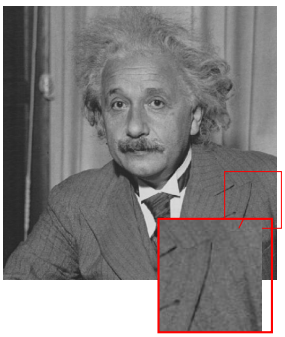

(a) Original image

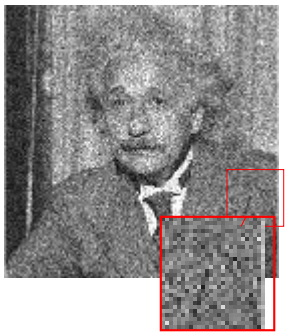

(b) peak = 55

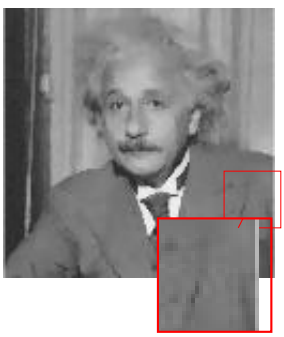

(c) TV [19]

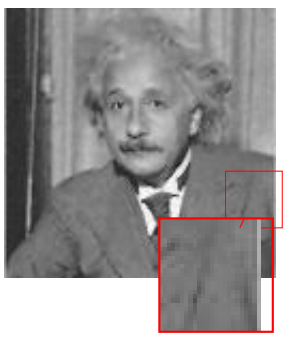

(d) TV^{α} model [27]

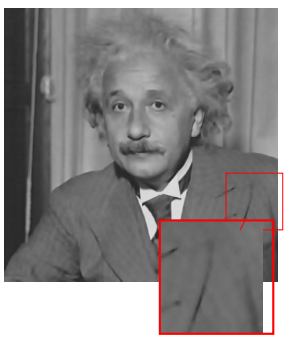

(e) Our approach

Figure 5: Comparison results of Poisson denoising using *Einstein image with peak at 55*

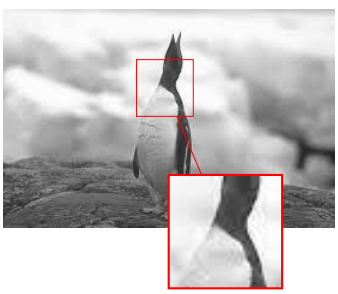

(a) Original image

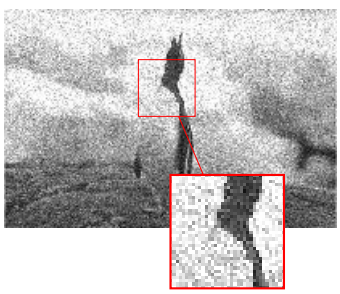

(b) peak = 55

(c) TV [19]

(d) TV^{α} model [27]

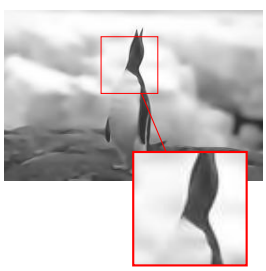

(e) Our approach

Figure 6: Comparison results of Poisson denoising using *Penguin image with peak at 55*

The Poisson denoising test results show the effectiveness of our model compared to the TV^{α} models. We assimilate the capability to preserve edges and corners of the original image, beside the robustness of the denoising process. As we can see, the proposed model reduces Poisson noise well while preserving important features, like the sharp edges and corners in the *Barbara and* Einstein images. Table (2) provides the quantitative results, listing the PSNR and SSIM values.

Table 2: PSNR and SSIM values records for different models.

image	Peak	TV [28]	TV^{α} [27]	proposed
Barbara	55	PSNR=24.42 SSIM=0.78	PSNR=25.87 SSIM= 0.81	PSNR= **26.98** SSIM= **0.87**
	155	PSNR=27.20 SSIM=0.84	PSNR= 29.14 SSIM=0.89	PSNR= **30.02** SSIM=**0.91**
	255	PSNR=29.27 SSIM=0.89	PSNR= 30.78 SSIM= 0.92	PSNR= **31.49** SSIM=**0.94**
Cameraman	55	PSNR=26.67 SSIM=0.80	PSNR=28.15 SSIM= 0.87	PSNR= **29.28** SSIM= **0.90**
	155	PSNR=28.55 SSIM=0.83	PSNR= 30.90 SSIM=0.92	PSNR= **31.75** SSIM=**0.94**
	255	PSNR=29.88 SSIM=0.87	PSNR= 32.31 SSIM= 0.94	PSNR= **33.22** SSIM=**0.96**

Our approach is mainly corrects the previous TV-based models drawbacks. The two regularizers rectify the common issues such as the Staicasing effects. In general, the robustness in the Poisson noise is rare, but our model shows a robustness against big values of noise (peak = 55). The suppression of the noise while preserving important features and details give our approach a great deal compared to the other models.

5. Conclusion

In this work, we proposed a model that combines two effective regularizers: variable-order Total Variation and anisotropic Total Variation. This combination successfully avoids common artifacts like staircasing and loss of contrast. We used the ADMM algorithm to solve the model and compared our approach to the standard TV model and a fractional TV^{α} model. Our method demonstrated strong performance, both visually and quantitatively. It effectively removes noise while preserving important edges and features. The quantitative results, presented in the table above, show higher PSNR and SSIM values than the competing models. For future work, we plan to explore using artificial neural networks (ANNs) to find optimal parameters and functions for the model.

References

1. Bai, J., Feng, X.-C., *Fractional-order anisotropic diffusion for image denoising*, IEEE transactions on image processing, 16(10), 2492–2502, (2007).

2. Berkels, B., Burger, M., Droske, M., Nemitz, O., Rumpf, M., *Cartoon extraction based on anisotropic image classification*, SFB 611, (2006).

3. Bonettini, S., Ruggiero, V., *An alternating extragradient method for total variation-based image restoration from poisson data*, Inverse Problems, 27(9), 095001, (2011).

4. Boyd, S., Parikh, N., Chu, E., *Distributed optimization and statistical learning via the alternating direction method of multipliers*, Now Publishers Inc, (2011).

5. Bredies, K., Kunisch, K., Pock, T., *Total generalized variation*, SIAM Journal on Imaging Sciences, 3(3), 492–526, (2010).

6. Chan, R. H., Setzer, S., Steidl, G., *Inpainting by flexible haar-wavelet shrinkage*, SIAM Journal on Imaging Sciences, 1(3), 273–293, (2008).

7. Chan, T., Marquina, A., Mulet, P., *High-order total variation-based image restoration*, SIAM Journal on Scientific Computing, 22(2), 503–516, (2000).

8. Chen, D., Chen, Y., Xue, D., *Fractional-order total variation image denoising based on proximity algorithm*, Applied Mathematics and Computation, 257, 537–545, (2015).

9. El Yazidi, Y., Ellabib, A., Ouakrim, Y., *On the stabilization of singular identification problem of an unknown discontinuous diffusion parameter in elliptic equation*, Comput. Math. Appl. 97, 267–285, (2021).

10. El Yazidi, Y., Ellabib, A., *Augmented Lagrangian approach for a bilateral free boundary problem*, J. Appl. Math. Comput. 67(1), 69–88, (2021).

11. El Yazidi, Y., Ellabib, A., *An iterative method for optimal control of bilateral free boundaries problem*, Math. Methods Appl. Sci. 44(14), 11664–11683, (2021).

12. El Yazidi, Y., & Ellabib, A. *A fuzzy particle swarm optimization method with application to shape design problem.* RAIRO-Operations Research, 57(5), 2819-2832, (2023).

13. El Yazidi, Y., Zeng, S., *A splitting based method for the numerical identification of a nonlinear convection coefficient in elliptic equations*, Math. Comput. Simul. 235, 205–218, (2025).

14. Figueiredo, M. A., Bioucas-Dias, J. M., *Deconvolution of poissonian images using variable splitting and augmented lagrangian optimization*, In *2009 IEEE/SP 15th Workshop on Statistical Signal Processing*, 733–736, IEEE, (2009).

15. Hakim, A., Ben-Loghfyry, A., *A total variable-order variation model for image denoising*, AIMS Mathematics, 4(5), 1320–1335, (2019).

16. Holla Kayyar, S., Jidesh, P., *Non-local total variation regularization approach for image restoration under a poisson degradation*, Journal of Modern Optics, 65(19), 2231–2242, (2018).

17. Laghrib, A., Ben-Loghfyry, A., Hadri, A., Hakim, A., *A nonconvex fractional order variational model for multi-frame image super-resolution*, Signal Processing: Image Communication, 67, 1–11, (2018).

18. Lant'eri, H., Theys, C., *Restoration of astrophysical images—the case of poisson data with additive gaussian noise*, EURASIP Journal on Advances in Signal Processing, 2005(15), 1–14, (2005).

19. Le, T., Chartrand, R., Asaki, T. J., *A variational approach to reconstructing images corrupted by poisson noise*, Journal of mathematical imaging and vision, 27(3), 257–263, (2007).

20. Liu, X., Huang, L., *Total bounded variation-based poissonian images recovery by split bregman iteration*, Mathematical Methods in the Applied Sciences, 35(5), 520–529, (2012).

21. Lysaker, M., Lundervold, A., Tai, X.-C., *Noise removal using fourth-order partial differential equation with applications to medical magnetic resonance images in space and time*, IEEE Transactions on image processing, 12(12), 1579–1590, (2003).

22. Macias, M., Sierociuk, D., *An alternative recursive fractional variable-order derivative definition and its analog validation*, In *ICFDA'14 International Conference on Fractional Differentiation and Its Applications 2014*, 1–6, IEEE, (2014).

23. Malesza, W., Macias, M., Sierociuk, D., *Matrix approach and analog modeling for solving fractional variable order differential equations*, In *Advances in Modelling and Control of Non-integer-Order Systems*, 71–80, Springer, (2015).

24. Patnaik, S., Hollkamp, J. P., Semperlotti, F., *Applications of variable-order fractional operators: a review*, Proceedings of the Royal Society A, 476(2234), 20190498, (2020).

25. Podlubny, I., *Fractional differential equations: an introduction to fractional derivatives, fractional differential equations, to methods of their solution and some of their applications*, Elsevier, (1998).

26. Pu, Y., *Fractional calculus approach to texture of digital image*, In *2006 8th international Conference on Signal Processing*, IEEE, (2006).

27. Rahman Chowdhury, M., Zhang, J., Qin, J., Lou, Y., *Poisson image denoising based on fractional-order total variation*, Inverse Problems & Imaging, 14(1), (2020).

28. Rudin, L. I., Osher, S., Fatemi, E., *Nonlinear total variation based noise removal algorithms*, Physica D: nonlinear phenomena, 60(1-4), 259–268, (1992).

29. Sierociuk, D., Malesza, W., Macias, M., *On the recursive fractional variable-order derivative: equivalent switching strategy, duality, and analog modeling*, Circuits, Systems, and Signal Processing, 34(4), 1077–1113, (2015).

30. Sierociuk, D., Twardy, M., *Duality of variable fractional order difference operators and its application in identification*, Bulletin of the Polish Academy of Sciences. Technical Sciences, 62(4), (2014).

31. Tikhonov, A. N., Goncharsky, A., Stepanov, V., Yagola, A. G., *Numerical methods for the solution of ill-posed problems*, Springer Science & Business Media, (2013).

32. Vardi, Y., Shepp, L., Kaufman, L., *A statistical model for positron emission tomography*, Journal of the American statistical Association, 80(389), 8–20, (1985).

33. Weickert, J., *Anisotropic diffusion in image processing*, Teubner Stuttgart, (1998).

34. Wen, Y., Chan, R. H., Zeng, T., *Primal-dual algorithms for total variation based image restoration under poisson noise*, Science China Mathematics, 59(1), 141–160, (2016).

35. Zhang, J., Chen, K., *A total fractional-order variation model for image restoration with nonhomogeneous boundary conditions and its numerical solution*, SIAM Journal on Imaging Sciences, 8(4), 2487–2518, (2015).

[1] *MSPASI, University of Hassan II of Casablanca, Faculty of sciences and technology, Morocco*

[2] *Research Laboratory of Numerical Analysis, Nonlinear Analysis, and Applications (LaR2A),*

Faculty of Sciences, Abdelmalek Essaadi University, Tetouan, Morocco.

E-mail address: anwarbenloghfyry@gmail.com, y.elyazidi@uae.ac.ma